

**Sputtering Flux Measurements
in the ASDEX Divertor**

G. Fussmann, J.V. Hofmann, G. Janeschitz, H.R. Yang*

IPP III /153 , Oct. 1989



MAX-PLANCK-INSTITUT FÜR PLASMAPHYSIK

8046 GARCHING BEI MÜNCHEN

MAX-PLANCK-INSTITUT FÜR PLASMAPHYSIK
GARCHING BEI MÜNCHEN

Sputtering Flux Measurements
in the ASDEX Divertor

G. Fussmann, J.V. Hofmann, G. Janeschitz, H.R. Yang*

IPP III/153, Oct. 1989

Abstract : Eroded copper fluxes from the target plates in the ASDEX divertor were measured spectroscopically. The measuring method is outlined and comprehensive experimental material for various modes of tokamak operation is presented. Assuming thermal sputtering to be the only erosion process, we find good agreement between code predictions and the measurements.

* On leave from South-Western Institute of Physics, Leshan, P.R. of China

Die nachstehende Arbeit wurde im Rahmen des Vertrages zwischen dem Max-Planck-Institut für Plasmaphysik und der Europäischen Atomgemeinschaft über die Zusammenarbeit auf dem Gebiete der Plasmaphysik durchgeführt.

Contents:

- 1. Introduction**
- 2. Principle of particle flux measurement**
- 3. Experimental results**
 - 3.1 Experimental arrangement
 - 3.2 Cu-flux profiles
 - 3.3 Parameter dependence of the target fluxes
- 4. Comparison with model calculations**
 - 4.1 2D simulation of the target plasma
 - 4.2. Discussion of numerical results
- 5. Summary**

1. Introduction

Design studies for reactor-like devices like NET and ITER [1] have particularly emphasized the importance of erosion of material at the divertor target plates. Huge amounts of material (tons of carbon per year) are predicted to be sputtered from the plates and redeposited in a largely unknown way. Despite the importance of these processes, little information is available from present experiments which can be regarded as a check of the underlying physics.

Some earlier results obtained from ASDEX have already been reported (see [2] to [4]). However, the method used to obtain these data and a comparison of the results with accompanying model calculations have not been presented so far. Both aspects will be covered in this paper (Secs. 2 and 4). In addition, more detailed information on sputtered Cu-fluxes - Cu being the target plate material of ASDEX - as a function of density, safety factor, and heating scenario are given in Sec. 3. On the other hand, we have omitted a discussion on divertor retention - a matter otherwise closely related to this topic - since most of the material available has already been presented in Ref. [4].

In Sec. 4 we describe a 2D model and a corresponding numerical code that takes into account the processes of sputtering, ionisation, and excitation of the neutrals in front of the target plate. Because of the strong inhomogeneities in this area, such a numerical code is indispensable for quantitative comparison with the measurements. The code is also used to calculate the redeposition profile on the target plate and the fraction of eroded particles that is deposited onto neighbouring surfaces.

2. Principle of particle flux measurements

There are two methods used for measuring particle fluxes emanating from selected surfaces: active laser-induced fluorescence (LIF) and passive spectroscopy. LIF is of advantage insofar as no information on temperature is needed, but otherwise it is a rather involved procedure.: A tuneable laser is required to excite the atoms in front of the surface, and two measurements (of the atomic density and streaming velocity) are

necessary to determine the particle flux $\Gamma = nv$. By comparison, passive spectroscopy provides a much simpler method since only absolute line intensities have to be measured. Accordingly, passive spectroscopy is the only practical method that allows investigations of flux patterns from extended particle sources.

The two methods were compared in the original ASDEX divertor configuration with titanium target plates. Satisfactory agreement within a factor of about 1.5 was found for the Ti-fluxes determined in the two ways [3].

In the following, we concentrate on the passive method which is basically applicable in all cases where the neutrals are ionized close to the emanating surface but do not recombine into the neutral state within the plasma. This condition is well satisfied in the majority of cases since electron temperatures of $T_e > 5$ eV are already attained in the outer scrape-off region and in the immediate proximity of the target plates. For the steady state the continuity equation for the neutrals in the ground state n_g^0 is then given by

$$\frac{\partial n_g^0}{\partial t} = -\text{div } \vec{\Gamma}_0 - n_e n_g^0 S_0 = 0, \quad (1)$$

where $\vec{\Gamma}_0$ is the neutral flux density, n_e the electron density, and $S_0 = \langle \sigma_{\text{ion}} v_e \rangle$ the ionization rate coefficient. Integrating equation (1) over the volume and applying Gauss's theorem leads to

$$\oint \vec{\Gamma}_0 \cdot d\vec{S} = \int n_e n_g^0 S_0 dV. \quad (2)$$

We now specify the volume as a box with area ΔS at the surface. The length of the box in the direction normal to the surface is chosen large in relation to the ionization length,

$$\lambda_{\text{ion}} = \frac{v_o}{S_o n_e} , \quad (3)$$

so that there is no outflux at the endsurface (v_o is the velocity of the neutrals).

Furthermore, if the flux density at the emanating surface is homogeneous over a scale length much larger than λ_{ion} , there will be no net flow through the side surfaces of the box either and equation (2) reduces to

$$\Gamma_o = \frac{1}{\Delta S} \int n_e n_g^o S_o dV , \quad (4)$$

where Γ_o is the input flux density averaged over the selected area ΔS .

It is now necessary to express the right-hand side of equation (4) in terms of the photon flux density measured by a spectrometer:

$$I_v = \frac{1}{\Delta S} \int \epsilon_v dV \quad (5)$$

with

$$\epsilon_v = \frac{h\nu}{4\pi} A_{mn} n_m^o \quad (6)$$

being the emissivity integrated over the frequency range of a particular line. Actually, I_v is the intensity measured in $\text{Wcm}^{-2} \text{ster}^{-1}$ or equivalent units. As a next step we invoke the so-called corona population equilibrium

$$n_m^o \sum A_{mn} = n_e n_g^o X_{gm} , \quad (7)$$

which states that the density n_m^o of level m is in equilibrium owing to electronic collisional excitation with rate X_{gm} from the ground state g and spontaneous decay into all lower levels n . Combining equations (7) and (6) and inserting the result for ϵ_v into equation (5) yields

$$I_v = \frac{h\nu}{4\pi} \frac{A_{mn}}{\Sigma A_{mn}} \frac{1}{\Delta S} \int n_e n_g^o X_{gm} dV . \quad (8)$$

Here the integral on the right-hand side very much resembles that needed in equation (4). The final connection is provided by extracting the rate coefficients from the integrals in both equations and replacing them by corresponding mean values \bar{S}_o and \bar{X}_{gm} . It should be noted that, because of $n_e n_g^o > 0$, these mean values are actually attained at a particular position within the considered volume. We thus obtain the fundamental relation

$$I_v = \frac{h\nu}{4\pi} \frac{A_{mn}}{\Sigma A_{mn}} \cdot \frac{\bar{X}_{gm}}{\bar{S}_o} \Gamma_o , \quad (9)$$

which links the particle flux density with the intensity via the branching ratio $B = A_{mn} / \Sigma A_{mn}$ and the ratio of excitation to ionization $P = B X_{gm} / S_o$. The latter quantity P is the corona approximation for the probability of photon emission per ionization event, which is actually required. P is still a function of temperature and approximately an exponential with respect to the parameter $\gamma = (E_{ion} - E_m) / kT_e$. The desired weak dependence on T_e is thus obtained for $\gamma \ll 1$ only. In principle, this could be achieved by choosing excitation levels E_m close to the ionization energy E_{ion} . In practice, however, such a choice is generally not permitted because of a possible break-down of the corona approximation on the one hand, and the need for high sensitivity, i.e. large B and X_{gm} / S_o ratios, on the other. For this reason, one is generally bound to strong resonance lines.

Behringer et al. [5] investigated the situation for the elements C, O and Cr, Fe, Ni in more detail by taking into account collisional redistribution among the excited levels and low-lying metastable levels. From their results presented for O^+ we learn that the normalized population density $n_m / (n_e n_g)$ of the 3s, 3p, 3d - 4P levels ($E_m / E_{ion} \approx 0.7$), generally used for oxygen flux measurements in the visible range, are practically density-independent for $n_e \leq 10^{13} \text{ cm}^{-3}$. Even up to $n_e = 10^{16} \text{ cm}^{-3}$ the variations are

quite marginal, i. e. less than a factor of about 2.5. In contrast, other levels like 3d 4D that are not exited directly from the ground state (2s² 2p³ 4S) show a very pronounced density dependence and are therefore not suited to flux measurements.

There are, unfortunately, no such detailed investigations available for the case of copper, the material of the ASDEX divertor plates. On the other hand, the situation is considerably simpler for Cu⁰ in relation to other metals because of the isolated 4s electron (ground state 3d¹⁰ 4s ²S), which produces a lithium-like spectrum with strong doublet lines. Furthermore, there is only one deep-lying metastable state 3d⁹ 4s² ³P (E_m = 1.39 eV), the population of which can be assessed from the intensity of the line λ = 5105.5 Å (4s² ²D_{5/2} - 4p ²P_{3/2}). For comparison, in the case of Fe⁰ there are four such states and no particularly strong lines but only hundreds of weak ones. The Cu⁰-fluxes are most easily determined from the strongest resonance line λ = 3247.5 Å (4s ²S_{1/2} - 4p ²P_{3/2}). For this line we calculated the probability P = X_{gm} B / S₀ as a function of T_e. The ionization rate is taken according to Lotz [6]; for excitation we use van Regemorter's formula

$$X_{gm} = \frac{1.6 \cdot 10^{-5} f_{gm} \langle g \rangle}{\Delta E_{gm}} \frac{e^{-\frac{\Delta E_{gm}}{T_e}}}{\sqrt{T_e}} \left(\frac{\text{cm}^3}{\text{s}} \right) \quad (10)$$

with ΔE_{gm} and T_e in eV and an average Gaunt factor of < g > = 0.8. The oscillator strength f_{gm} determined for this transition from live time measurements [7] is 0.439. The resulting function P(T_e) is plotted in Fig. 1. The branching ratio B for this line is 1.

3. Experimental results

3.1 Experimental arrangement

The geometry of the ASDEX divertor and the experimental set-up used for measuring the eroded fluxes from the target plate is sketched in Fig. 2. Only the bottom divertor

region including the lower X-point of the separatrix is shown in the figure. The separatrix intersects the divertor plates at a grazing angle of about 30° . The outer branch of the separatrix can be observed through a slit 5 cm wide and 10 cm high in the water-cooled shielding enclosing the core region of the divertor. The surface of the neutralizer plates is optimized for high power fluxes along the field lines by means of a shallow sawtooth-like structure with a period length of 2 cm in the toroidal direction [8]. This structure must be noted in Cu-flux measurements since they are obtained from the UV-light emitted by a narrow rectangular surface only 0.2 cm wide. The intensity variation caused by the periodic structure is found to be about $\pm 50\%$ deviation from the average for the most and least exposed parts of the surface. Observations can be made either directly or via a scanning mirror. The mirror allows on a shot-to-shot basis a scan over the total target plate and the divertor throat region. Without the mirror only a range about 6 cm high is accessible on the lower part of the plate. The separatrix position can be shifted vertically by changing the ratio of the plasma current I_P to the divertor current in the multipole coils I_M . The best plasma performance is found for a ratio of $I_M / I_P = 8 \times 0.085 = 0.68$, where the separatrix is everywhere more than ~ 1.5 cm away from the metallic walls in the throat region.

The light produced in the divertor region is conducted out of the tokamak via a quartz window and focused onto the entrance slit of a 1m spectrometer by a single quartz lens. In case the scanning mirror is not used, the second of the two mirrors shown in Fig.2 is tilted until the viewing line hits the target plate directly. As detector, a multichannel system (OMA) with a sensitive range of 1000 pixels (each $25 \mu\text{m} \times 2.5 \text{mm}$) is applied. The communication with the OMA camera is performed by a controller connected to a UNIX computer workstation (Fig. 2). This system allows graphical presentation and data management of up to 200 spectra per discharge with an integration time of 20 ms for each spectrum. The OMA detector can be used in the spectral mode, or - by turning it 90° - in the spatially resolving mode. As an example of the spectral mode we show in Fig. 3 the temporal evolution of the spectrum around the prominent Cu I doublet. Obviously, the two lines of the $2S - 2P$ doublet completely dominate the spectrum. Although the intensity changes quite substantially on account of additional heating, the intensity ratio I_{3247} / I_{3274} stays constant at ~ 1.95 , i.e. very close to the expected ratio of the f-values of 2.0.

3.2. Cu-flux profiles

An example of a spatial mode measurement is presented in Fig. 4 (without scanning mirror). In this case the spectrometer is set to the resonance wavelength $\lambda = 3247 \text{ \AA}$. The intensity versus the height of the exit slit ($\sim 1 \text{ cm}$) is then a de-magnification of the emission pattern at the divertor plate. In Sec. 4 we will show that the observed light is essentially produced within a very short distance of a few mm from the plate surface. The peak maximum in Fig. 4 therefore gives us a rather accurate measurement of the separatrix position. This determination is facilitated by a secondary light peak from a small reflecting surface in the divertor providing a precise position marker (Fig. 4). The agreement with the position of the separatrix calculated from magnetic measurements, $\Delta Z = 0.7 \text{ cm}$, is quite satisfactory; it is already close to the physical uncertainty of a few mm for the coincidence between maximum of sputtering and separatrix position imposed by cross diffusion processes.

Careful calibration of the whole system is a prerequisite for reliable flux measurements. For this purpose we placed a tungsten ribbon lamp in front of the divertor plates and reduced the spectrometer entrance area ($h \cdot s$) so that only light from the homogeneous part of its surface was detected. The ribbon lamp was used under normal incidence at a black-body temperature of $T_S = 2500 \text{ K}$ at $\lambda = 4000 \text{ \AA}$, corresponding to a true tungsten temperature of $T_W = 2656 \text{ K}$. From the Kirchhoff-Planck function we thus calculate a calibration emissivity of $L_c = 8.08 \cdot 10^{-6} \text{ W / (ster} \cdot \text{cm}^2 \cdot \text{\AA)}$ at $\lambda = 3247 \text{ \AA}$. The solid angle in the calibration as well as in the experiments is determined by the area of the spectrometer grating ($\Omega_c = \Omega = A/f^2 = 10^{-2}$) which is completely illuminated in all cases. The absolute intensity is finally obtained from the relation

$$I = (L_c \cdot \Delta\lambda_{\text{pix}}) \cdot \frac{\sum \dot{N}_K}{\dot{N}_c} \cdot \frac{(h \cdot s)_c}{(h \cdot s)} \cdot \frac{\Omega_c}{\Omega} \cdot \frac{1}{\cos \alpha}, \quad (11)$$

where the index c refers to the calibration values ($\dot{N}_c = \text{counts/pixel/s}$). The sum $\sum \dot{N}_K$ is the count rate integrated over the spectral range of the line. $\Delta\lambda_{\text{pix}}$ is the wavelength per pixel (0.203 \AA) and α is the angle of the detected light beam to the normal of the target plate.

3.3 Parameter dependence of target fluxes

From a physical point of view sputtering fluxes should be discussed first of all in terms of the leading parameters: local temperatures (T_i, T_e) and densities (n_i, n_e). These quantities, however, are not routinely available on ASDEX, and, moreover, the corresponding measurements from Langmuir probes (n_e, T_e) and impurity Doppler broadening (T_i) are also to some extent questionable with regard to their applicability to the erosion processes. We postpone these questions to the next section and confine ourselves here to empirical relations that describe the fluxes in terms of well-defined secondary parameters such as the line-averaged density of the main plasma (\bar{n}_e), safety factor q , as well as the power and type of additional heating. There are other parameters such as the ion mixing in the divertor region (background ions H^+ , D^+ , and impurities: mainly C^{n+} and O^{n+} with $n \leq 3$) or surface conditioning of the target plates which are found to be of importance, too, but which are only qualitatively known. For this reason functional relations can be obtained in a reliable way from shot series only where the conditioning of the tokamak does not change.

In Fig. 5 we present Cu^0 -flux densities as a function of \bar{n}_e with the neutral injection heating power (P_{NI}) as a parameter. The upper four curves refer to D^0 injection ($E_{max} = 50$ keV, $P_{NI} = 0.6, 1.05, 1.65, 2.1$ MW) into D^+ plasmas with L-mode confinement under non-carbonized wall conditions. The dotted curve underneath shows the result for H^0 injection ($P_{NI} = 1.3$ MW, L-mode) into D^+ plasmas after carbonization. Finally, the lowest curve (dashed) is for pure ohmic heating ($P_{OH} = 0.4$ MW) in D^+ . All flux densities shown in Fig. 5 and the following figures are peak values for divertor double null operation; they refer to the separatrix position in the dip region of the sawtooth modulated surface (Sec. 3.1). For the intensity to flux density conversion a fixed reference temperature of $T_e = T_i = 12.5$ eV (as determined by previous Doppler broadening measurements of CIII-lines [3]) was assumed for the adjacent plasma region. By means of equation (9) we obtain the relation $\Gamma_0 = (5.18 \cdot 10^{18} I)$ $cm^{-2} s^{-1}$ with I in W/cm^2 . Flux contributions from Cu-neutrals in the 3P metastable level (Sec. 2) are estimated from the $\lambda = 5106$ Å line emission to be 30% at maximum. This contribution is neglected throughout this paper because of its relatively large uncertainty and since the above-mentioned line had been measured in a few cases

only. The solid curves for D⁰ injection shown in Fig. 5 and the pure ohmic case (dashed) can be fitted to an accuracy of about 20% by the formula

$$\Gamma_o = (\Gamma_{OH} + C \cdot P_{NI}) \cdot \bar{n}_e^{-1.7}, \quad (12)$$

where $\Gamma_{OH} = 0.55 \cdot 10^{16} \text{ cm}^{-2} \text{ s}^{-1}$, $C = 9.2 \cdot 10^{16} \text{ cm}^{-2} \text{ s}^{-1}$ and with P_{NI} and \bar{n}_e given in MW and 10^{13} cm^{-3} , respectively. The linear dependence with respect to the neutral injection power P_{NI} in equation (12) is demonstrated in Fig. 6. For this series of shots an almost quadratic decay with density \bar{n}_e is thus found. In contrast, there is no such dependence under carbonized conditions (dotted curve in Fig. 5). One possible explanation for this strange behaviour may be given by enhanced radiation cooling on account of large carbon influxes at low densities. Strong indications of enhanced carbon influxes under these conditions are found from Z_{eff} bremsstrahlung measurements, yielding values of Z_{eff} as high as 4-6 in the edge region. Furthermore, the sputtering level for this case of H⁰ injection is much lower than those for D⁰ injection at the same power. Such a strong dependence on the injection mass appears to be a systematic one (see below).

Similar power studies have also been performed for ICRH and for combined ICRH and NI heating in D⁺ plasmas. In Fig. 7 we present raw data of Cu I-intensities as a function of time for a series of shots with two separate NI phases of fixed power and superposed ICRH. The two NI phases differ in the species injected (1st phase H⁰, 2nd phase D⁰), but are otherwise comparable in power ($P_{NI}(\text{H}^0) = 1.0 \text{ MW}$, $P_{NI}(\text{D}^0) = 1.2 \text{ MW}$). While the density is unchanged at $\bar{n}_e = 3.44 \cdot 10^{13} \text{ cm}^{-3}$, the ICRH power is changed from shot to shot up to 2.5 MW.

From the trace $P_{ICRH} = 0$ shown in Fig. 7 we learn again that D⁰ injection causes about twice as much Cu-sputtering as H⁰ injection. This difference cannot be attributed to the higher sputtering yield of deuterium since the injected particles are of minor importance within the total particle balance; hence the majority of particles streaming onto the divertor plates are deuterons in any case. The different sputtering efficiency is more likely caused by higher ion temperatures in the edge and divertor regions in the

case of D° injection. This interpretation is supported by other observations, e.g. the lower power threshold for achieving the H-mode in case of D° injection.

Of further interest is the tendency of sputtering to overshoot with the onset of NI heating. This phenomenon is particularly pronounced for high-power D° injection (Fig. 7). To our understanding, this behaviour is attributable to the long time constants involved in achieving steady state conditions in the divertor. The reduction of the sputtering fluxes is thus a consequence of approaching the high recycling condition characterized by a high-density, low-temperature target plasma.

In Fig. 8 the dependence of the sputtered Cu-flux densities is plotted versus the ICRH power for the three phases (ICRH + H° -NI, pure ICRH, ICRH + D° -NI) indicated in Fig. 7. Although time averaging over relatively large intervals (0.2 s) was applied for the first and third phases, a large scatter in the data is still observed. Nevertheless, a linear dependence with approximately equal slopes $\Gamma_0 / P_{ICRH} = 0.56 \cdot 10^{16} \text{ cm}^{-2}\text{s}^{-1} / \text{MW}$ is clearly resolved for the three phases from regression analysis. This slope is only about half of the corresponding one for D° -NI at the same density ($\Gamma_0 / P_{NI} = 1.0 \cdot 10^{16} \text{ cm}^{-2}\text{s}^{-1} / \text{MW}$). On the other hand, comparing the 1 MW point of pure ICRH in Fig. 8 with the point on axis for $P_{ICRH} = 0$ of the middle curve, we conclude that ICRH and H° -NI have about equal sputtering efficiency.

A rather unexpected result is shown in Fig. 9, where the sputtered Cu-flux densities are plotted as a function of the safety factor q for ohmic D^+ discharges. The variable used in Fig. 9 is actually the cylindrical approximation of the safety factor neglecting the divertor field, $q = q_a = a B_{\phi} / R_0 B_{\theta}$; its variation is accomplished by changing the toroidal field B_{ϕ} only. The three curves shown in Fig. 9 belong to two different densities ($\bar{n}_e = 2.8$ and $3.3 \cdot 10^{13} \text{ cm}^{-3}$) and two plasma currents ($I_p = 380$ and 350 kA). The two upper curves belong to the same lower density but differ in I_p ; they show a strong dependence on q according to $\Gamma_0 \propto q^{-2.5}$. The lower curve in Fig. 9 for the higher density ($I_p = 380 \text{ kA}$, $\bar{n}_e = 3.3 \cdot 10^{13} \text{ cm}^{-3}$) shows a weaker but still remarkable dependence on q ($\Gamma_0 \propto q^{-1.4}$).

Although a quantitative understanding of the observed q -dependence is still lacking, qualitative arguments can be invoked by referring to the connection length between the main plasma and divertor plate along the field lines, which scales proportionally to q . With increasing connection length, however, plasma cooling on account of re-

ionization processes of neutrals in the divertor region becomes more efficient and thus reduces target erosion.

From the peak flux densities shown in the figures, the total fluxes Φ_0 cannot be determined without making further assumptions about toroidal symmetry and the contributions from the remaining two inner target plates and the outer one in the upper divertor. Relevant information on these questions is now being obtained from calorimetric power deposition measurements in the 4 x 8 octants of the plates [9]. Pronounced toroidal asymmetries of up to a factor of two have been found, which to some extent may be attributed to slight misalignment of the multipole coils [10]. On the other hand, the degree of symmetry is not constant but also changes with the operation conditions, and is largest during LH heating. At the toroidal position (NE sector) where our measurements are made the power loading is in general slightly above average. Furthermore, the power flux onto the outer plates is about twice as large as onto the inner ones. This effect is taken into account by the multiplier 3 in the equation below:

$$\Phi_0 \approx 3 \cdot (2\pi R) \cdot \left(\frac{3}{4} \Gamma_0\right) \cdot \Delta Z_{eq} \approx \Gamma_0 \cdot 7.1 \cdot 10^4 \text{ s}^{-1}, \quad (13)$$

The surface modulation is taken into account by an averaging factor 3/4; ΔZ_{eq} is the equivalent width of the sputtering flux profile, which is found to be about 2.5 cm by integrating $\Gamma_0(z)$ over z . Total Cu-erosion fluxes thus range from about $0.7 \cdot 10^{20} \text{ s}^{-1}$ for ohmic discharges to $25 \cdot 10^{20} \text{ s}^{-1}$ in low-density ($2.8 \cdot 10^{13} \text{ cm}^{-3}$) D^o-heated (2.5 MW) plasmas.

4. Comparison with model calculations

The spectroscopic method outlined in Sec. 2 and applied in Sec. 3 is based on the assumption that the plasma is homogeneous over the ionisation length defined by equation 3. This assumption is only marginally justified - and breaks down for very low density conditions - because of the strong temperature and density gradients

perpendicular to the separatrix. There is therefore need for a more refined description that takes these facts into account. Such 2D modelling of the plasma sheath in front of the target plate is required in particular to assess the quality with which the measured intensity profiles represent the actual erosion profiles.

First we describe the numerical model developed for this purpose and then discuss some typical results in Sec. 4.2.

4.1 2D simulation of the target plasma

The processes taking place in front of the divertor plate are described in a two-dimensional space: x and z are the coordinates perpendicular and parallel (in the vertical direction) to the plate as shown in Fig. 10. For convenience we refer in the following to the geometry of the upper divertor. No variations in the y -direction are considered here owing to the toroidal symmetry. Along the z -axis the plate extends from $-L/2$ to $+L/2$ (with $L \approx 8$ cm in ASDEX). The separatrix intersects the plate at $z = 0$ and is - within the small geometrical range considered - approximated by a circle of radius $r_s = 20$ cm with its centre at (x_c, z_c) . The intersection angle with the plate surface is not normal but typically 30° . The temperature and density are assumed to be functions only of the distance to the separatrix,

$$D(x,z) = \sqrt{(x - x_c)^2 + (z - z_c)^2} - r_s, \quad (14)$$

but they depend on the sign of D , too.

Furthermore, we approximate the density $n = n_e = n_i$ and temperature $T = T_e = T_i$ by exponential fits

$$n = n_s e^{-|D|/\lambda_n^+}, \quad (15a)$$

$$T = T_s e^{-|D|/\lambda_T^+}, \quad (15b)$$

where the decay lengths are different for the inner region ($D < 0$: $\lambda_n^- \approx \lambda_T^- \approx 0.5$ cm) and outer region ($D > 0$: $\lambda_n^+ \approx 2$ cm, $\lambda_T^+ \approx 4$ cm). The incoming flux density of the background ions is calculated from

$$\Gamma_i = n_i v_i B_{\text{pol}}/B_{\text{tor}} , \quad (16a)$$

with v_i being the sound velocity

$$v_i = \sqrt{\frac{8 T_i}{3 m_i}} . \quad (16b)$$

$B_{\text{pol}} / B_{\text{tor}} \approx 0.1$ takes into account the angle of incidence of the field lines in the toroidal direction.

The above ion flux produces a sputtering flux

$$Q = \Gamma_i Y_{\text{Cu}} , \quad (17a)$$

where the sputtering yield for copper is approximated in the range $10 \text{ eV} < T < 100 \text{ eV}$ by a power law

$$Y_{\text{Cu}} = \left(\frac{T}{T^*} \right)^\alpha \quad (17b)$$

The constants α and T^* were obtained from published results [4] for protons ($\alpha = 4.66$, $T^* = 90.1 \text{ eV}$) and deuterons ($\alpha = 4.33$, $T^* = 51.3 \text{ eV}$) including the additional acceleration by the sheath potential.

Inserting expressions (15), (16) and (17b) into equation (17a), we obtain for the impurity source function at the plate ($x = 0$)

$$Q(z_p) = \frac{B_{\text{pol}}}{B_{\text{tor}}} \sqrt{\frac{8 T_s}{3 m_i}} \left(\frac{T_s}{T^*}\right)^\alpha n_s \cdot e^{-z_p \left[\frac{1}{\lambda_n} + \left(\frac{1}{2} + \alpha\right) \frac{1}{\lambda_T} \right]}, \quad (18)$$

where the vertical source coordinate z_p has been introduced to make a distinction from the free space coordinate z .

In agreement with sputtering measurements [11] we assume a sputtering distribution function proportional to $\cos \theta$, with θ being the angle with respect to the normal of the plate surface (x -direction). With attenuation neglected at this stage, the flux from the surface element $dA_p = dz_p dy_p$ emitted into the solid-angle $d\Omega = \sin \theta d\theta d\phi$ is then given by

$$d^2\Phi = \frac{Q}{\pi} \cos(\theta) d\Omega dA_p. \quad (19)$$

Normalization has been chosen in such a way that integrating the above expression over a half sphere yields a total flux density equal to Q :

$$\frac{d\Phi}{dA_p} = \frac{Q}{\pi} 2\pi \int_0^{\pi/2} \cos(\theta) \sin(\theta) d\theta = Q. \quad (20)$$

The contribution of the surface element dA_p at point $Q (0, y_p, z_p)$ to the flux through a small sphere of cross-section dA at the position $P (x, 0, z)$ is analogously to equation (19) given by

$$d^2\Phi = \frac{Q}{\pi} \cos(\theta) \frac{dA}{QP^2} \exp\left(-\int_\alpha^P \frac{n_e S_0}{v_0} dl\right) dA_p, \quad (21)$$

with

$$\overline{QP} = \sqrt{x^2 + y_p^2 + (z - z_p)^2}, \quad (21a)$$

and

$$\cos \theta = \frac{x}{\overline{QP}}. \quad (21b)$$

In equation (21) a solid-angle of $d\Omega = dA / \overline{QP}^2$ is taken into account. This applies to non-directed flux densities (through a sphere) which are related to the density according to $\Gamma = n v_0$ where the velocity v_0 is also independent of the direction. As a further simplification we assume the same velocity for all neutrals

$$v_0 = \sqrt{\frac{2 E_{\text{sputt}}}{m_{\text{Cu}}}}. \quad (21c)$$

Attenuation due to ionisation is taken into account by the exponential term in equation (21). The total flux density at the position P is obtained by integrating over the plate surface

$$\Gamma(x, z) = \frac{d\Phi}{dA} = \iint \frac{Q}{\pi} \frac{x}{[x^2 + y_p^2 + (z - z_p)^2]^{3/2}} \exp\left(-\int_Q^P \frac{n_e S_0}{v_0} dl\right) dz_p dy_p. \quad (24)$$

Owing to the uniformity in the y-direction the integration over y_p can be performed explicitly. Introducing the distance to the surface point $Q_0 (0, 0, z_p)$

$$l_0 = \overline{Q_0P} = \sqrt{x^2 + (z - z_p)^2} \quad (25)$$

and $\eta = y_p/l_0$ we obtain

$$\Gamma(x, z) = \int_{-L/2}^{+L/2} dz_p \frac{Q}{\pi} \frac{x}{l_0^2} \int_{-\infty}^{+\infty} d\eta \frac{\exp(-\tau_0 \sqrt{1 + \eta^2})}{[1 + \eta^2]^{3/2}}, \quad (26)$$

which may be written as

$$\Gamma(x,z) = \int_{-L/2}^{+L/2} \frac{2 Q(z_p)}{\pi} \frac{x}{x^2+(z-z_p)^2} M(\tau_0) dz_p, \quad (27)$$

with

$$\tau_0 = \int_{Q_0}^P \frac{n_e S_0}{v_0} dl_0. \quad (27a)$$

For the transparency function $M(\tau_0)$ we found a useful approximation (accuracy better than 7 % in the range $0 \leq \tau_0 \leq 10$)

$$M(\tau_0) = \int_0^{\infty} \frac{e^{-\tau_0 \sqrt{1+\eta^2}}}{(\sqrt{1+\eta^2})^3} d\eta \approx e^{-\tau_0 - \frac{1}{3}\sqrt{\tau_0}}. \quad (28)$$

The remaining calculations are facilitated by introducing the angle γ in the x-z plane according to

$$\cos(\gamma) = \frac{x}{l_0}. \quad (29)$$

The "optical depth" τ_0 is then transformed by means of $dl_0 = dx'/\cos(\gamma)$ and $z' = z_p + x' \tan(\gamma)$ to

$$\tau_0(x, \gamma) = \frac{1}{v_0 \cos \gamma} \int_0^x n_e(x', z') S_0(x', z') dx'. \quad (30)$$

Finally the neutral density is obtained from $n_0 = \Gamma/v_0$ to

$$n_0(x, z) = \frac{2}{\pi v_0 x} \int_{-L/2}^{L/2} Q(z_p) \cos^2(\gamma) M(-\tau_0(x, \gamma)) dz_p. \quad (31)$$

The limit value $x \rightarrow 0$ for approaching the plate is more easily derived from equation (27) with $M=1$. We obtain

$$n_0(x=0, z) = \frac{2 Q(z)}{\pi v_0} \int_{-\infty}^{+\infty} \frac{d\zeta}{1+\zeta^2} = \frac{2 Q(z)}{v_0} . \quad (32)$$

It should be noted that the corresponding flux density $\Gamma(x=0) = 2Q$ is just twice as large as according to equation (20). The factor of two is again due to the difference between directed and non-directed fluxes. We would retain the result of equ. 20) by considering fluxes through an oriented surface $d\vec{A} = dA \vec{e}_x$ which would call for another factor $\cos\theta$ in equation (21).

With the neutral density now calculated, it is a straightforward matter to calculate the photon emissivity by using the expressions given in Sec. 2:

$$\varepsilon = \frac{h\nu}{4\pi} n_o n_e X(T_e) \cdot B . \quad (33)$$

For comparison with the measured intensity profiles, however, a further integration, according to equation (8), along the specified lines of sight has to be performed.

Similarly to the emissivity in equation (33), the ion production rate

$$\frac{\partial n_{Cu}^+}{\partial t} = - \frac{\partial n_o}{\partial t} = n_o n_e S_o \quad (34)$$

can also be calculated. Assuming that these ions - apart from a small fraction leaking towards the main plasma - are swept towards the target plate along the same magnetic surface on which they are born, we can easily obtain the re-deposition profile on the plate $Q^+(z_p)$ by integrating n_{Cu}^+ between circles of constant distance $D = r - r_s$.

A two-dimensional numerical code (PLATE) was developed that allows us to obtain computational results of the sputtering fluxes Q , the Cu-neutral density distribution n_0 , the re-deposition profile Q^+ , and, finally, the intensity profile when observing the plate at an angle α with respect to its normal. Cartesian coordinates with a typical mesh width of 0.25 cm are used. Integrations are performed by applying the trapeze rule for $n_0(z)$ and $Q^+(z_p)$. The sensitive transparency function $M(\tau_0)$, however, is calculated by using a 12-point Gauss procedure for eq. (30) with corresponding inter-mesh points.

4.2 Discussion of numerical results

As input data for numerical simulations we use Langmuir probe measurements in the divertor [12]. The application of these n_e and T_i measurements remains uncertain to some extent because they cannot be performed in the immediate vicinity of the plate but at a distance of ~ 10 cm, i.e. about 1 m apart along the field lines. For a typical low-density D^+ discharge ($\bar{n}_e = 2.8 \cdot 10^{13} \text{ cm}^{-3}$, $I_p = 320 \text{ kA}$, #24579) the measured density and temperature profiles are depicted in Fig. 11 as a function of the plate coordinate z_p . The exponential fittings for the inner and outer regions as given by equation (15) are also shown. The values at the separatrix amount to $n_s = 4.6 \cdot 10^{12} \text{ cm}^{-3}$, $T_s = 14.6 \text{ eV}$; the decay lengths are $\lambda_n^+ = 2.2 \text{ cm}$, $\lambda_n^- = 0.6 \text{ cm}$, $\lambda_T^+ = 4.0 \text{ cm}$, $\lambda_T^- = 0.5 \text{ cm}$. Calculating the ionisation length from equation (3) for the separatrix values - which actually provides a lower limit - we obtain $\lambda_{\text{ion}} = 0.4 \text{ cm}$ (assuming $E_{\text{sputt}} = 1.5 \text{ eV}$) which is already of the same order as the above decay length. The sputtered flux density profile for copper atoms (equation (18)) is shown for the cited conditions in Fig. 12. Assuming the same temperatures and densities for H^+ and D^+ plasmas the much higher sputtering yield of deuterons is obvious from the figure.

Contour plots of constant neutral Cu density n_0 (equation (31)) are presented in Figs. 13 and 14. Figure 13 is the result obtained for the cited conditions. At the intersection point $x = z = 0$ the maximum Cu density is found from equation (32) to be $6.1 \cdot 10^{10} \text{ cm}^{-3}$. We notice from Fig. 13 that less than 5% of the particles reach the indicated shielding plate (hatched line) facing the target surface. Figure 13 also demonstrates the up-down asymmetry introduced by the divertor plasma, which streams from below towards the $x = z = 0$ intersection point. The Cu-atoms therefore have a much larger free range in the $+z$ -direction, i.e. away from the main plasma. The situation

appreciably changes when the electron density is artificially lowered by a factor of 10 to $n_e = 4.6 \cdot 10^{11} \text{ cm}^{-3}$, as shown in Fig. 14. Under such conditions the Cu-atoms are no longer well retained in the plasma region but have a probability of more than 10% of being deposited on the shielding plate. Taking further into account that with decreasing n_e the temperature, and thus the sputtering rate, rises, we conclude that the considerable Cu deposits found on the shielding plates of ASDEX are produced preferentially in very low density operation a frequent condition on ASDEX for LH current drive studies.

The comparison between the calculated and measured intensity profiles $I(z_p)$ is shown in Fig. 15. In this case the measured profile was taken by means of a scanning mirror (Fig. 2) and evaluated according to equation (11) with $\alpha = 37^\circ$. Apart from the somewhat higher current (380 kA instead of 320 kA) the discharge parameters (# 23419 - 23424, D^+ , $\bar{n}_e = 2.8 \cdot 10^{13} \text{ cm}^{-3}$) fit to those cited above. To allow a better comparison of the profile shape, the calculated values were multiplied by a factor of 1.4. The agreement in shape and in particular in magnitude is excellent. It should be mentioned that the intensity profile significantly differs in shape and width from the sputtering profile shown in Fig. 12. The peak position still coincides, however, with the separatrix intersection position, as was tacitly assumed in Sec. 3.2.

Finally, we compare in Fig. 16 the calculated ionic re-deposition profile $Q^+(z_p)$ with the erosion profile $Q(z_p)$. Owing to the already mentioned up-down asymmetry the re-deposition profile is shifted by about $\Delta z_p = 1.5 \text{ cm}$ in the direction away from the main plasma.

5. Summary

The spectroscopic method of flux measurement was applied to determine the eroded fluxes from the ASDEX divertor plate. This method is very convenient and could be used to obtain profiles of the Cu-fluxes as a function of time. A certain shortcoming of the procedure is the relatively pronounced dependence on the electron temperature (Fig.1), which, for a quantitative analysis, must be known within an uncertainty of approximately 50%.

Local flux densities in the range $0.3\text{-}3 \times 10^{16} \text{ Cu-atoms/cm}^2$ were measured for additionally heated D^+ discharges. As mentioned above the accuracy in these

absolute measurements is largely determined by the uncertainty of T_e and is estimated at approximately 50-100%. The fluxes show a sensitive dependence with respect to the line-averaged density of the main plasma and the safety factor (Figs. 5,9). Furthermore, they increase linearly with auxiliary heating power with about equal slopes for ICRH and H^0 injection (Figs. 5,6,8). In the case of D^0 injection, however, the sputtering rates are approximately two times higher.

Because of the strong T_i -dependence of the sputtering yield, the erosion profiles are very narrow, showing half-widths of 1-2 cm. These widths refer to an intersection angle of 30° of the separatrix with the surface of the plate. For normal incidence even narrower profiles are to be expected.

On average, the eroded neutral Cu-atoms are rapidly ionized in the adjacent divertor plasma and have a short range of typically 0.5 cm only. Owing to the strong inhomogeneities of the density and temperature, however, a small fraction of the sputtered particles can have considerably larger ranges. For this reason the measured intensity profiles do not properly represent the flux profiles but are broader. The comparison with spectroscopic measurements therefore requires numerical simulation of the intensity profile based on measured temperature and density profiles. Performing such calculations (Sec.4), we find satisfying agreement between measurement and simulation, both for the profile shape and the absolute values. There is thus no necessity to invoke additional sputtering contributions from suprathermal plasma ions, as has previously been presumed [3]. On the other hand, it must be realized that there are numerous sources of uncertainties that enter in such comparisons (particularly T_i , n_e - profiles as well as sputtering contributions by impurities). The accuracy in the simulations is therefore much lower than the accuracy of flux measurements, and at present state is certainly not better than within a factor of two. Further investigations along the lines indicated in this paper are thus needed to improve the reliability of the conclusions drawn from such comparisons.

References

- [1] D. Post et al., 12th Int. Conf. on Plasma Physics and Controlled Nucl. Fusion Research, Nice, (1988)
- [2] B. Schweer et al., J. Nucl. Materials 111-112 (1982) 71
- [3] G. Fussmann, V. Ditte, W. Eckstein et al., J. Nucl. Materials 128-129 (1984), 350-358
- [4] J. Roth, G. Janeschitz et al., Nucl. Fus., to be published
- [5] K. Behringer, et al., JET-report JET-P(89)05, Jan.. 1989
- [6] W. Lotz, Astrophys. J. Suppl. 14, 207-238 (1967)
- [7] P. Hamaford, R.M. Love, 22, Opt. Eng. 532-544 (1983)
- [8] H. Niedermeyer, G. Becker, B. Bomba et al., Plasma Physics and Contr. Fusion, 30, 11, 1443-1453 (1988)
- [9] T. Evans and the ASDEX team," Measurements of Poloidal and Toroidal Energy Absorption Asymmetries in the ASDEX Divertors", IPP Report III / 154
- [10] J. Neuhauser, M. Bessenrodt-Weberpals, B.J. Braams et al., Plasma Physics and Controlled Fusion, 31, 10, 1551-1568 (1989)
- [11] J. Roth, J. Bohdanský, W. Ottenberger, "Data on Low Energy Light Ion Sputtering", Report IPP 9/26 (1979)
- [12] N.Tsois et al., Proc. 16th Europ. Conf. on Controlled Fusion and Plasma Physics, Vol.III , 907, Venice (1989)

Figure captions

Fig. 1 The ratio of photons per ionisation event for the Cu I resonance line $\lambda=3247.5 \text{ \AA}$ as a function of electron temperature.

Fig. 2 Experimental arrangement for spectroscopic flux measurements in the ASDEX divertor.

Fig. 3 Temporal evolution of the Cu I resonance doublet ($4s \text{ } ^2S_{1/2} - 4p \text{ } ^2P_{1/2,3/2}$) during a discharge with additional NI and ICRH heating (#25234, $P_{NI} = 2.1 \text{ MW}$, $P_{ICRH} = 1.5 \text{ MW}$).

Fig. 4 Measured Cu I intensity profile in front of the divertor plate during NI - heating . The vertical distance z is measured from the plasma centre. The position of the separatrix as calculated from magnetic measurements is also indicated (#26326 , $t=1.28 \text{ s}$, $P_{NI} = 1.2 \text{ MW}$, $H^0 \rightarrow D^+$, $I_M / I_p = 8 \times 0.085$).

Fig.5 Cu-flux density (peak) from the divertor plate vs. line-averaged density of the bulk plasma with NI heating power as a parameter. Curves from bottom to top : dashed = ohmic; dotted = carbonized, $H^0 \rightarrow D^+$ (1.3 MW); solid = $D^0 \rightarrow D^+$ ($P_{NI} = 0.6, 1.05, 1.65, 2.10 \text{ MW}$).

Fig 6 Cu-flux density vs. total power with \bar{n}_e as a parameter.

Fig. 7 Cu-flux density as a function of time with combined ICRH and NI heating ($H^0 \rightarrow D^+$ [1 MW] and $D^0 \rightarrow D^+$ [1.2 MW]). Note the substantially larger fluxes during the second D^0 injection phase.

Fig. 8 Cu- flux densities as a function of ICRH - power for discharges with additional NI - heating (see Fig.7).

Fig. 9 Cu-flux densities as a function of q with \bar{n}_e as a parameter for ohmic D⁺ discharges. Symbols: x : $3.3 \cdot 10^{13} \text{ cm}^{-3}$ [350kA] , ●●● : $2.8 \cdot 10^{13} \text{ cm}^{-3}$ [350 kA], ooo : $2.8 \cdot 10^{13} \text{ cm}^{-3}$ [380 kA].

Fig. 10 Divertor geometry used for numerical modelling. The separatrix is simplified by a circle with centre at point C. The density and temperature are taken as functions of the distance to the separatrix D (x,y).

Fig. 11 Semi-log-plots of the measured density and temperature profiles in the divertor. Triangles refer to $D < 0$, solid points to $D > 0$.

Fig. 12 Calculated Cu-sputtering flux profiles for protons and deuterons applying the temperature and density profiles shown in Fig. 11.

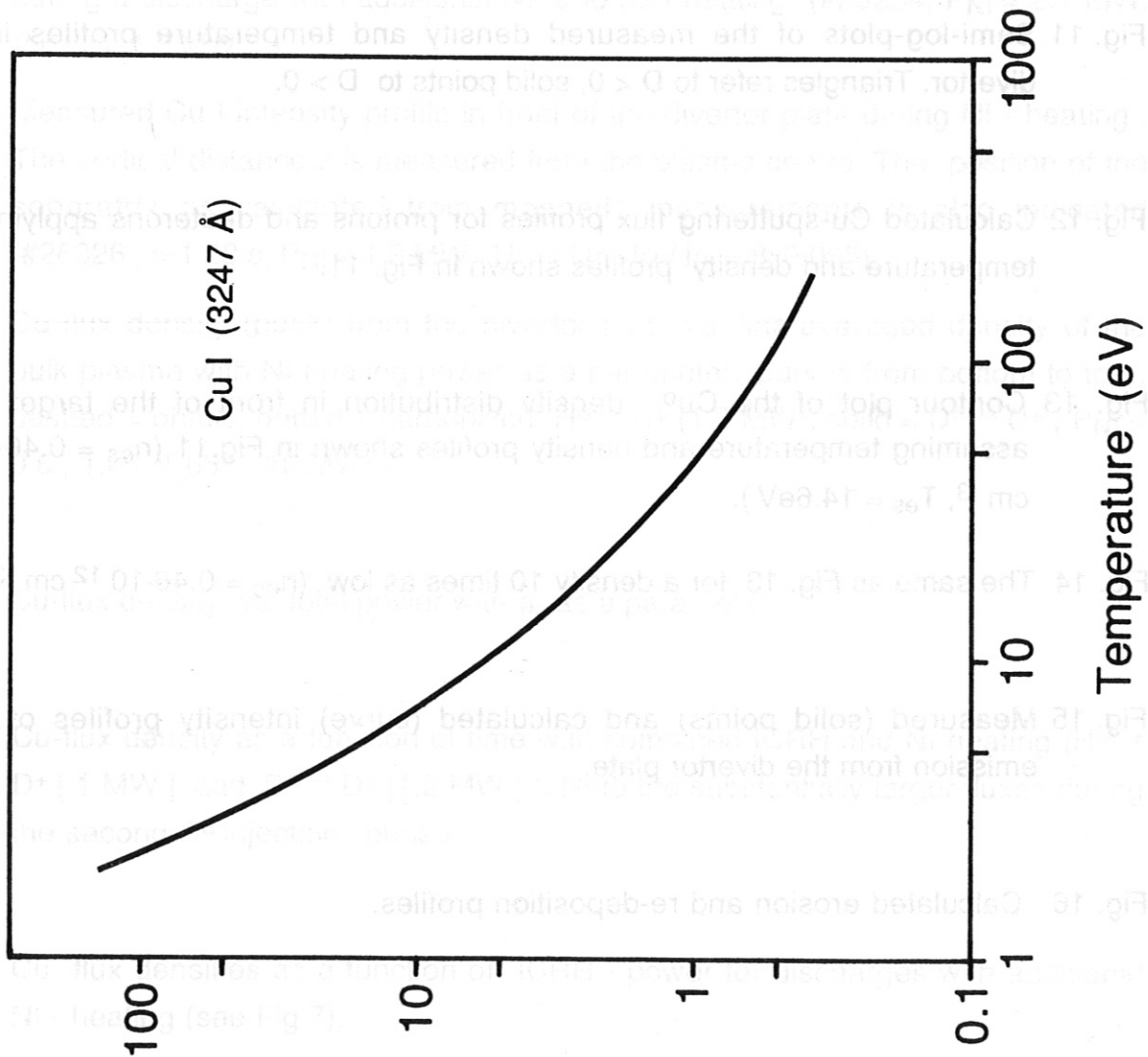
Fig. 13 Contour plot of the Cu⁰ - density distribution in front of the target plate assuming temperature and density profiles shown in Fig.11 ($n_{eS} = 0.46 \cdot 10^{13} \text{ cm}^{-3}$, $T_{eS} = 14.6 \text{ eV}$).

Fig. 14 The same as Fig. 13 for a density 10 times as low ($n_{eS} = 0.46 \cdot 10^{12} \text{ cm}^{-3}$).

Fig. 15 Measured (solid points) and calculated (curve) intensity profiles of Cu I emission from the divertor plate.

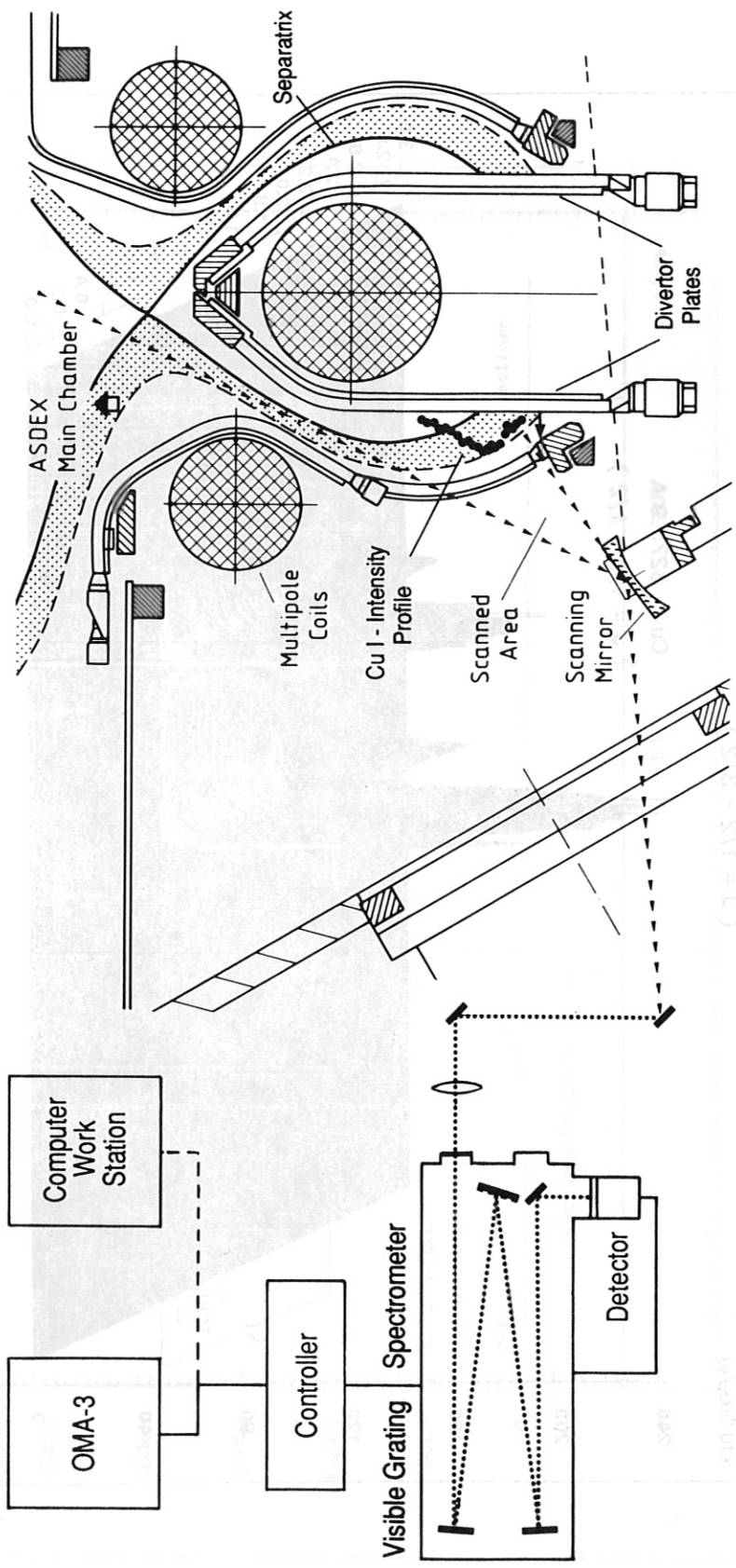
Fig. 16 Calculated erosion and re-deposition profiles.

Photons / Ionisation event (XB/So)



IPP 3 FSM 451 - 89

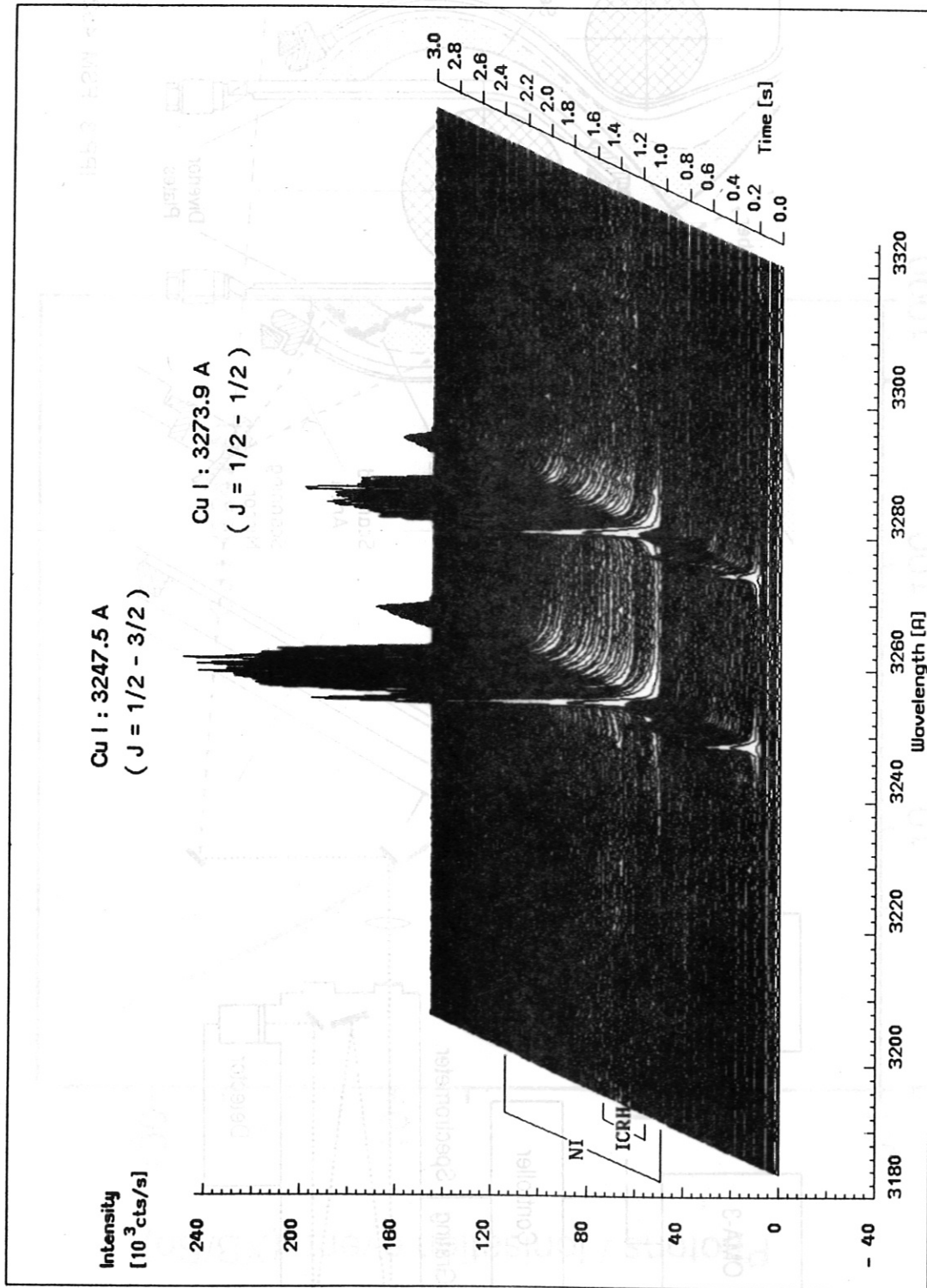
z.g. 1



IPP 3 FSM 452 - 89

ASDEX A 1218 E - 28ECLH0300A *** LYING: 3532 V 68' 1500' 2801: 52534

-- ASDEX VISIBLE SPECTROSCOPY --, LAMC: 3247 A, GR: 1200, SHOT: 25234

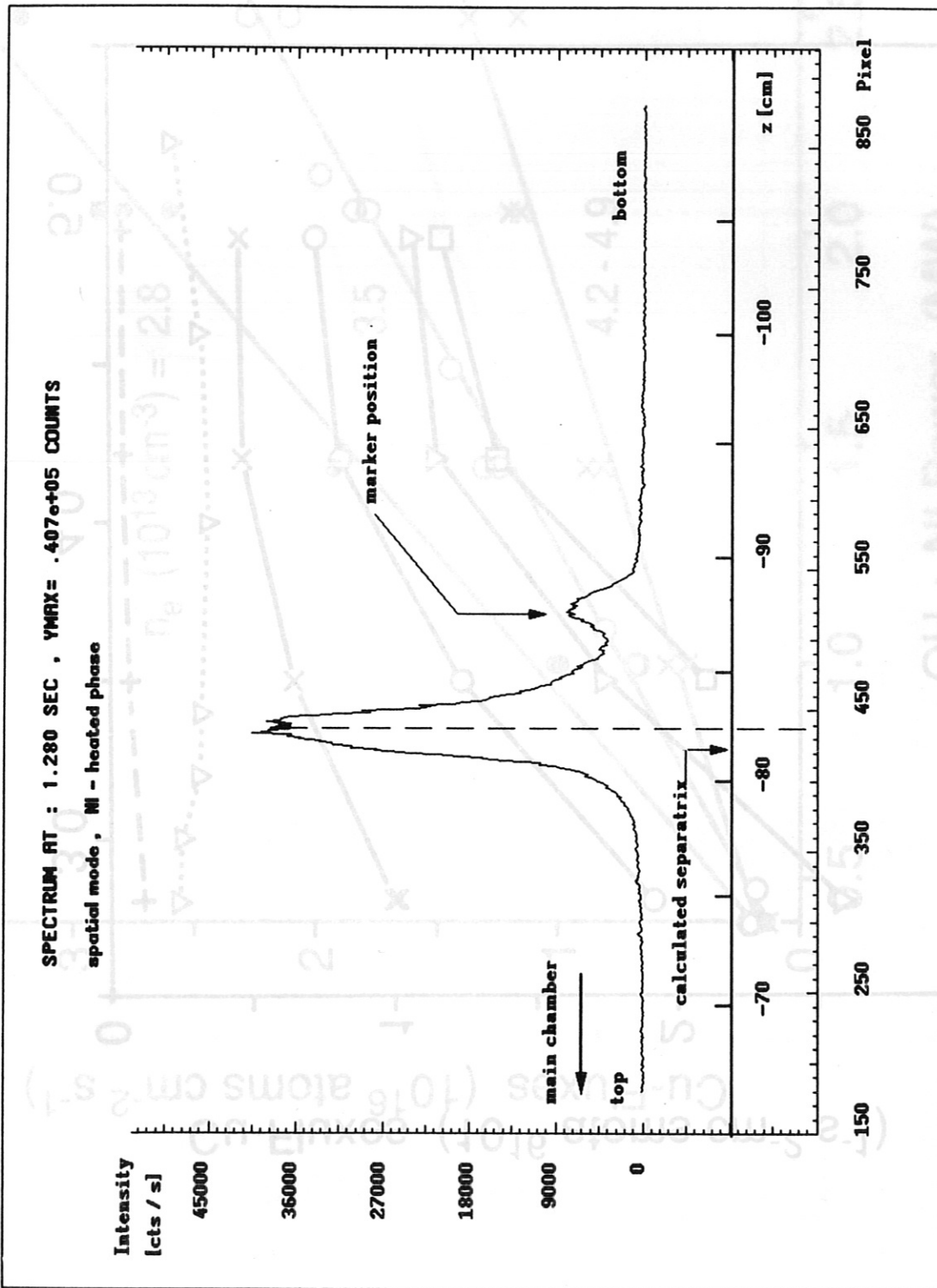


IPP 3 FSM 453 - 89

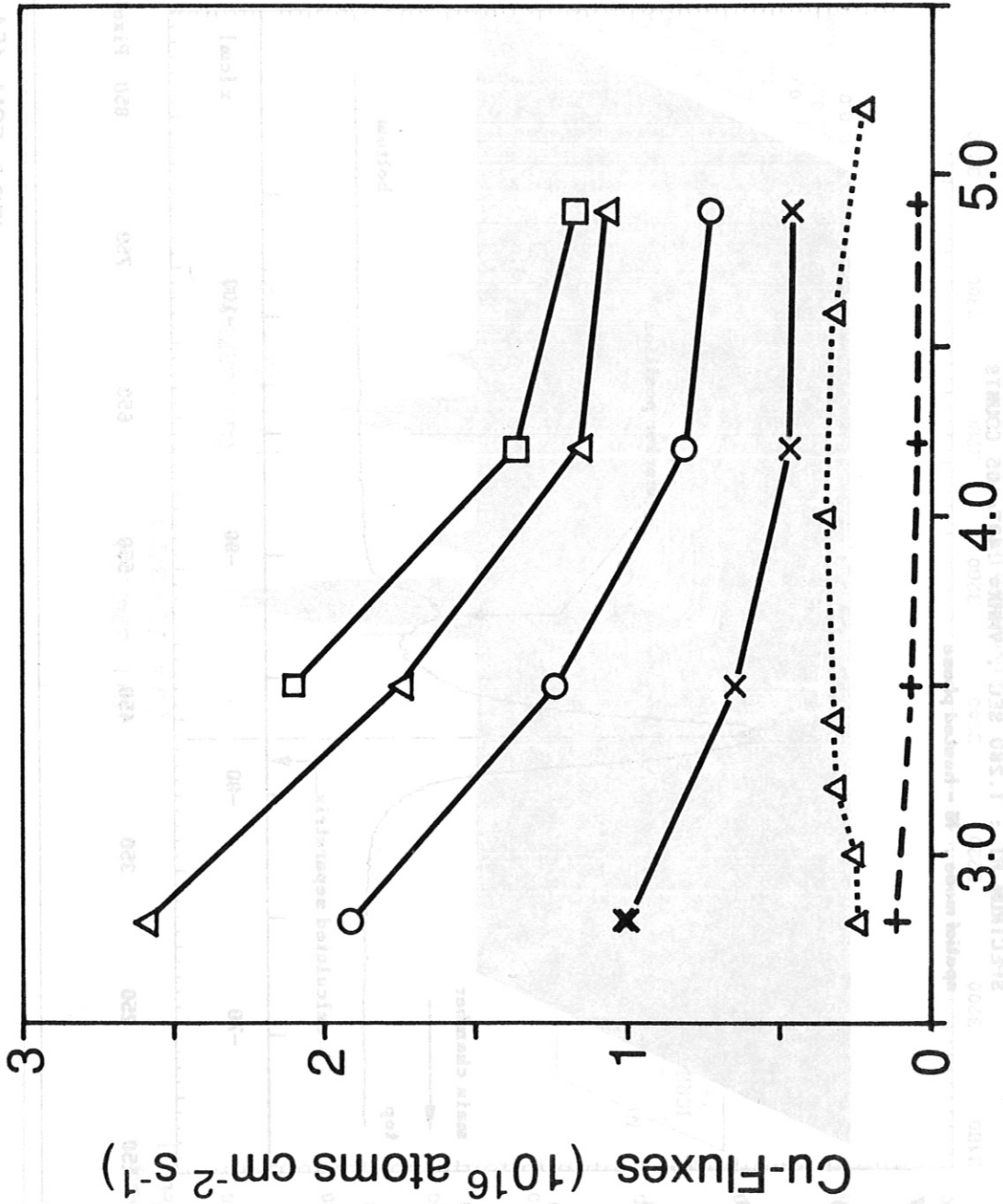
Fig. 3

.. ASDEX VISIBLE -SPECTROSCOPY .., LAMC: 3247 A, SHOT: 26326

DEIT_20.26326



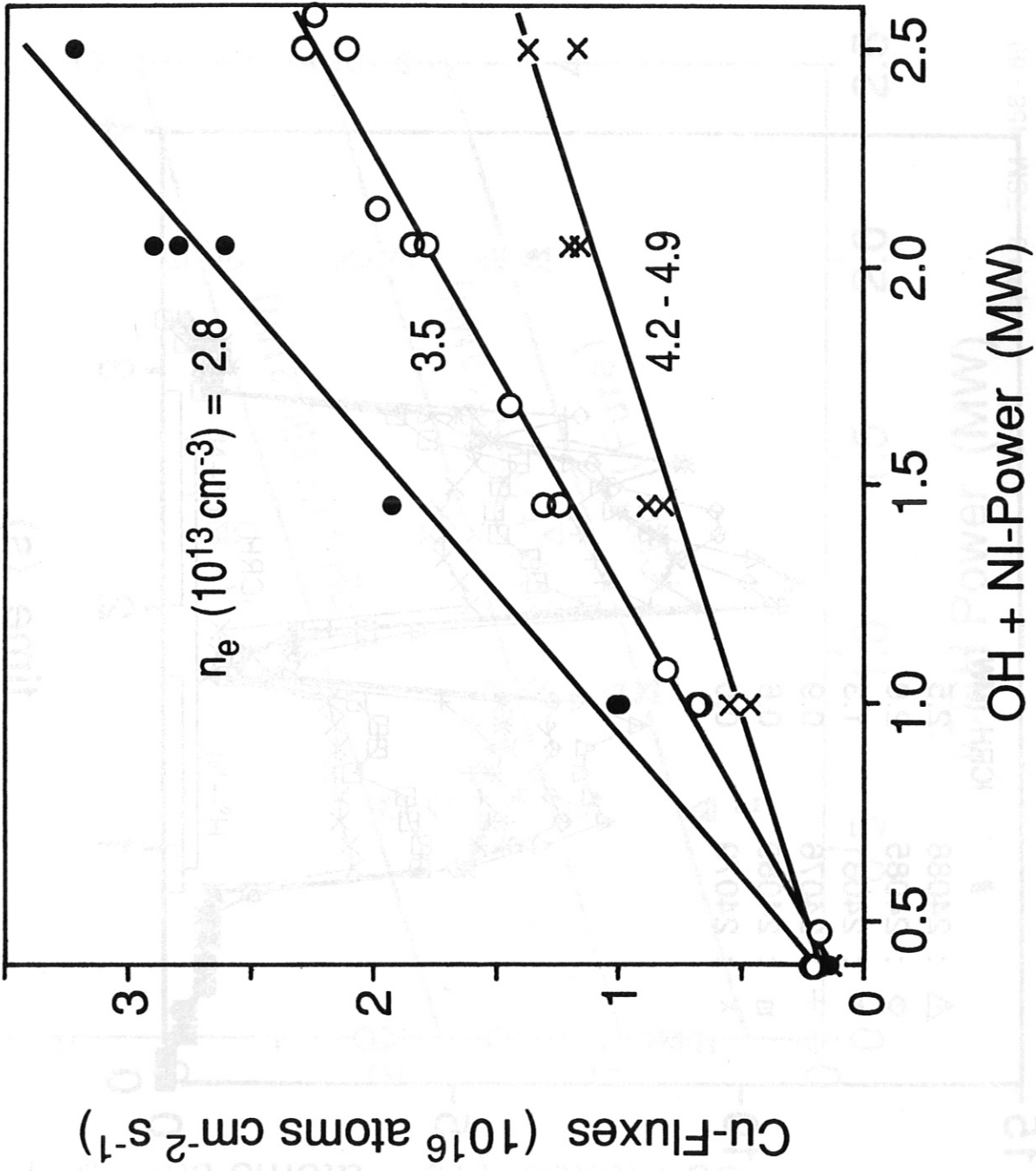
2.4.8

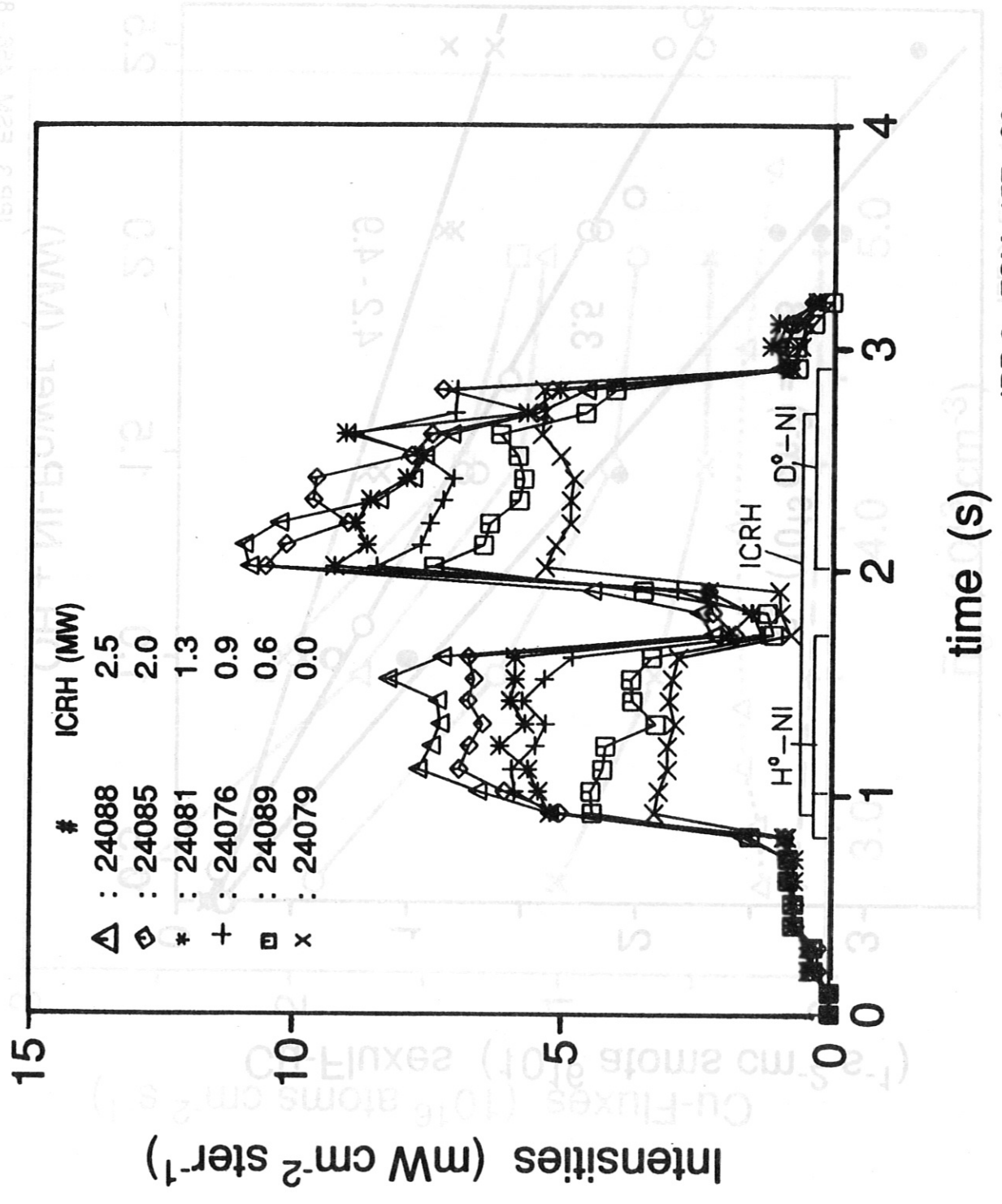


\bar{n}_e (10^{13} cm^{-3})

IPP 3 FSM 455 - 89

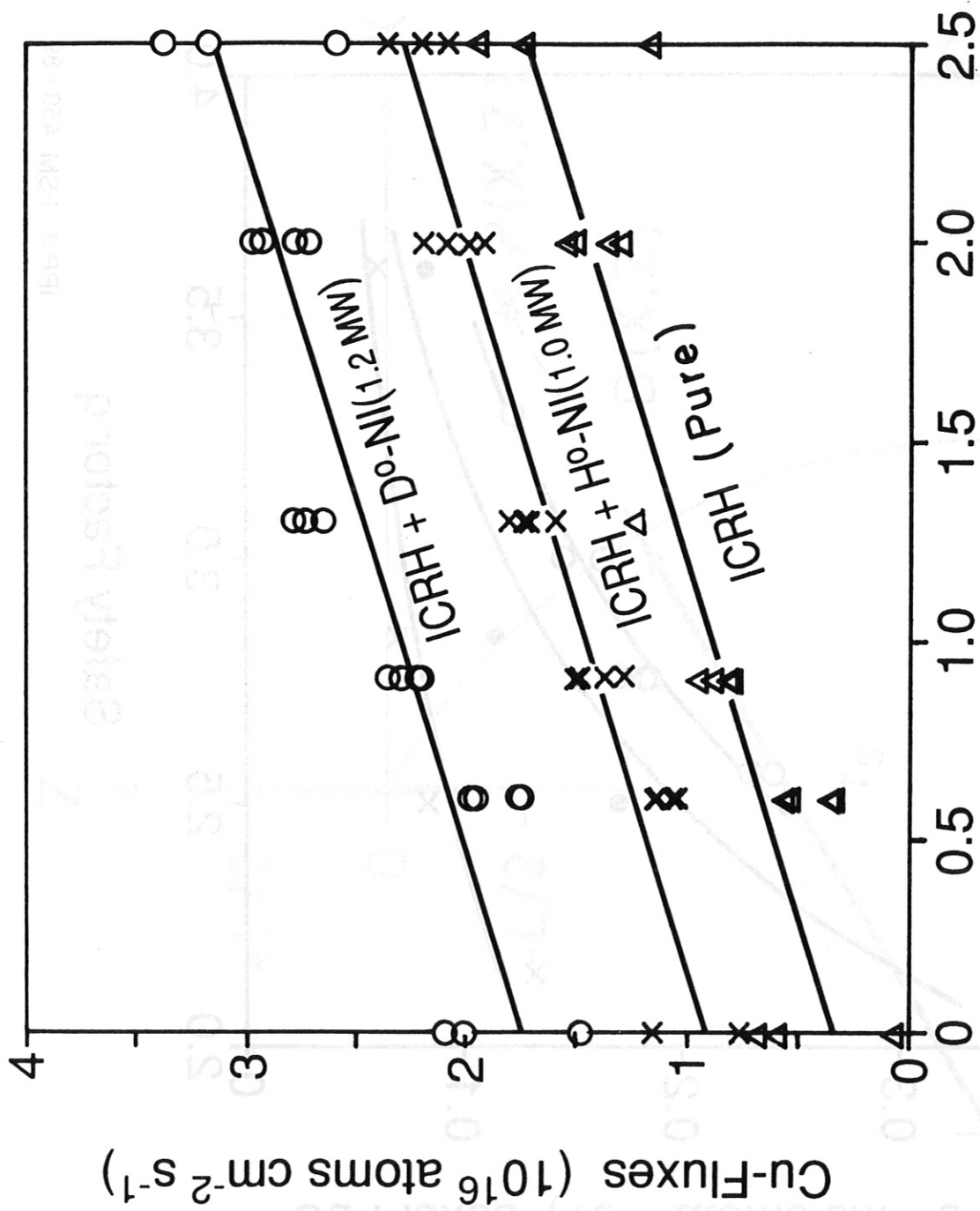
Fig. 5



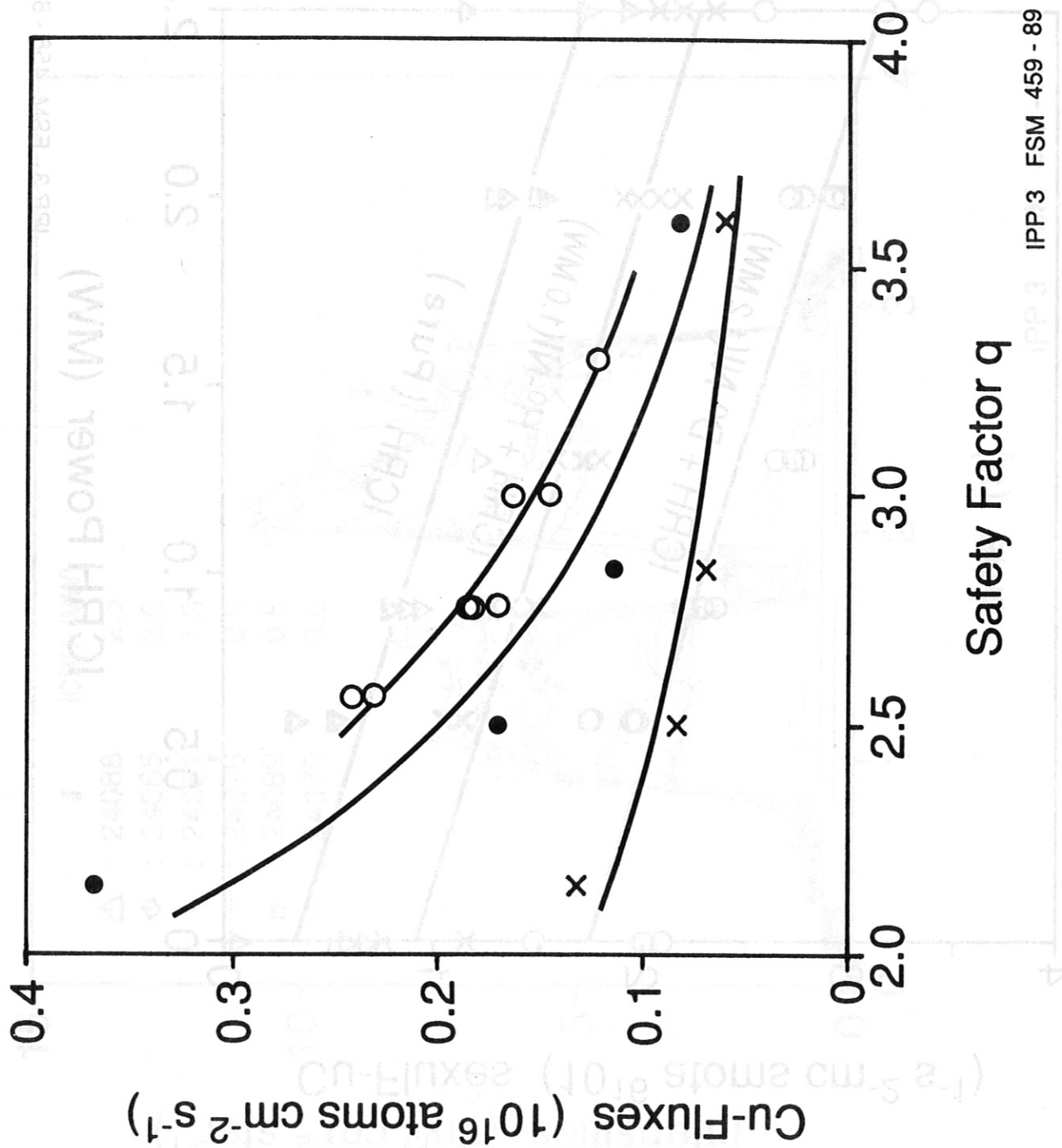


IPP3 FSM 457 - 89

Fig. 7



ICRH Power (MW)

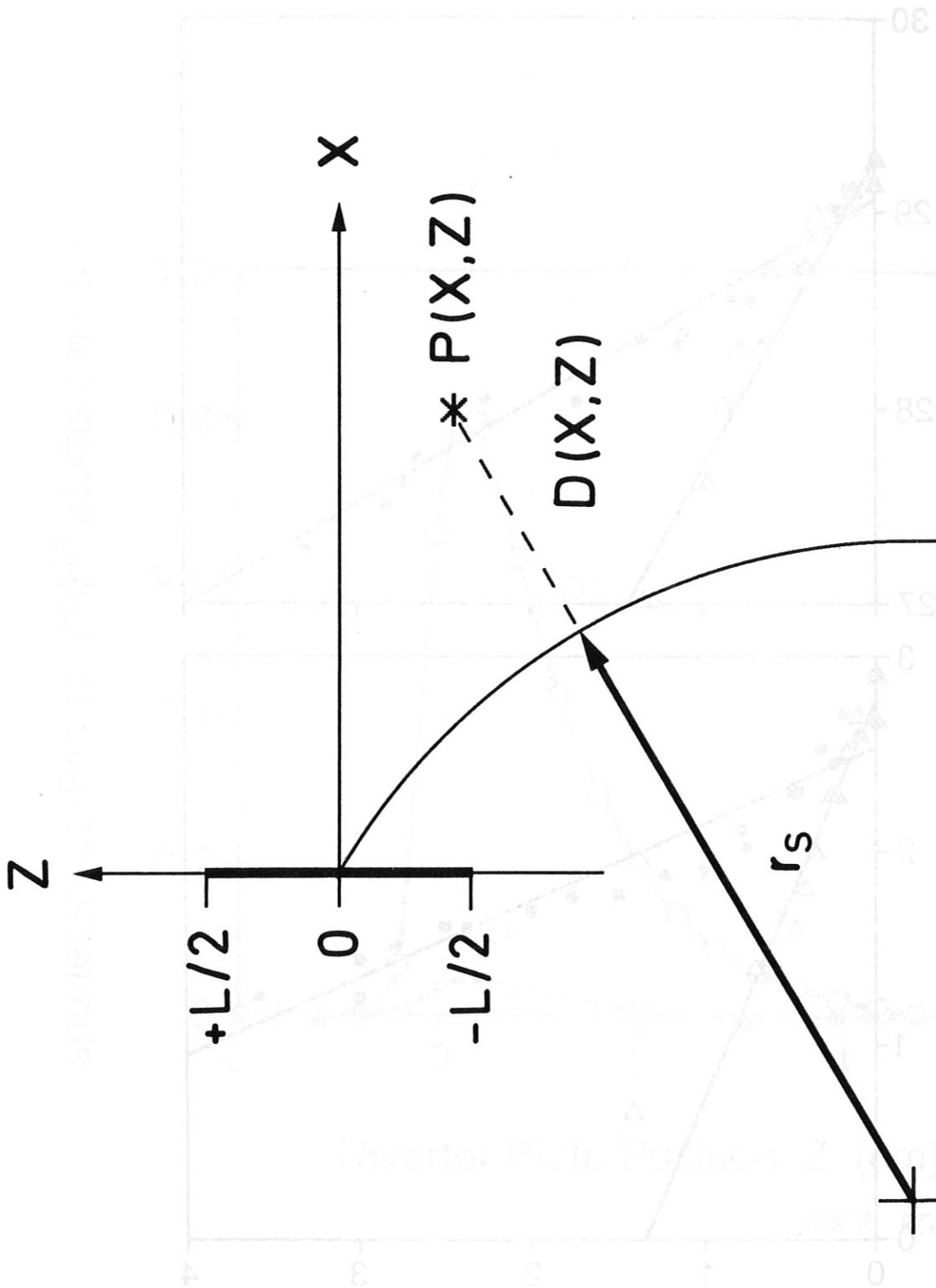


Safety Factor q

Fig. 9

IPP 3 FSM 459 - 89

IPP 3 FSM 459 - 89

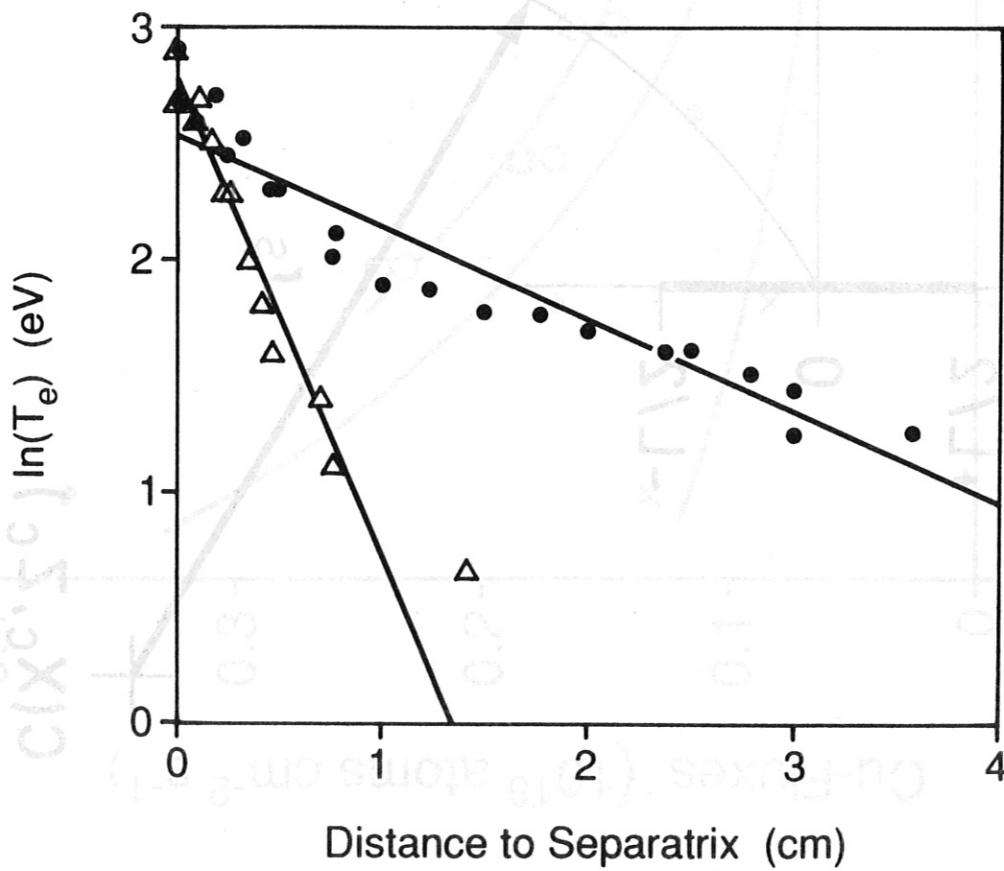
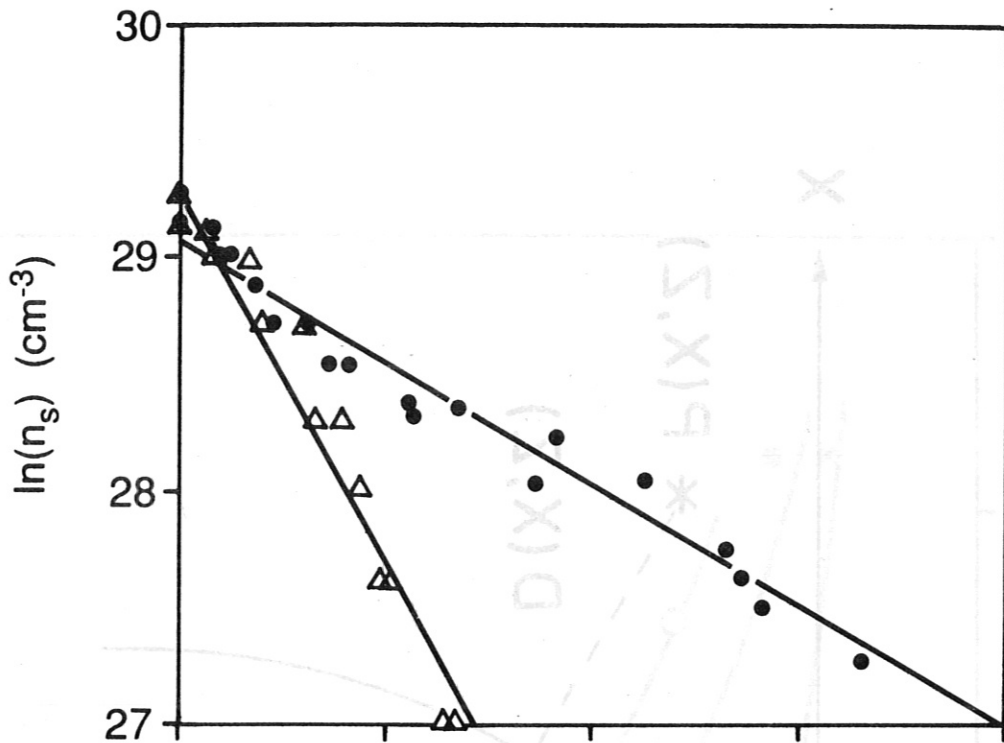


$C(X_c, Z_c)$

$\mu(u^2)$ (cm³)

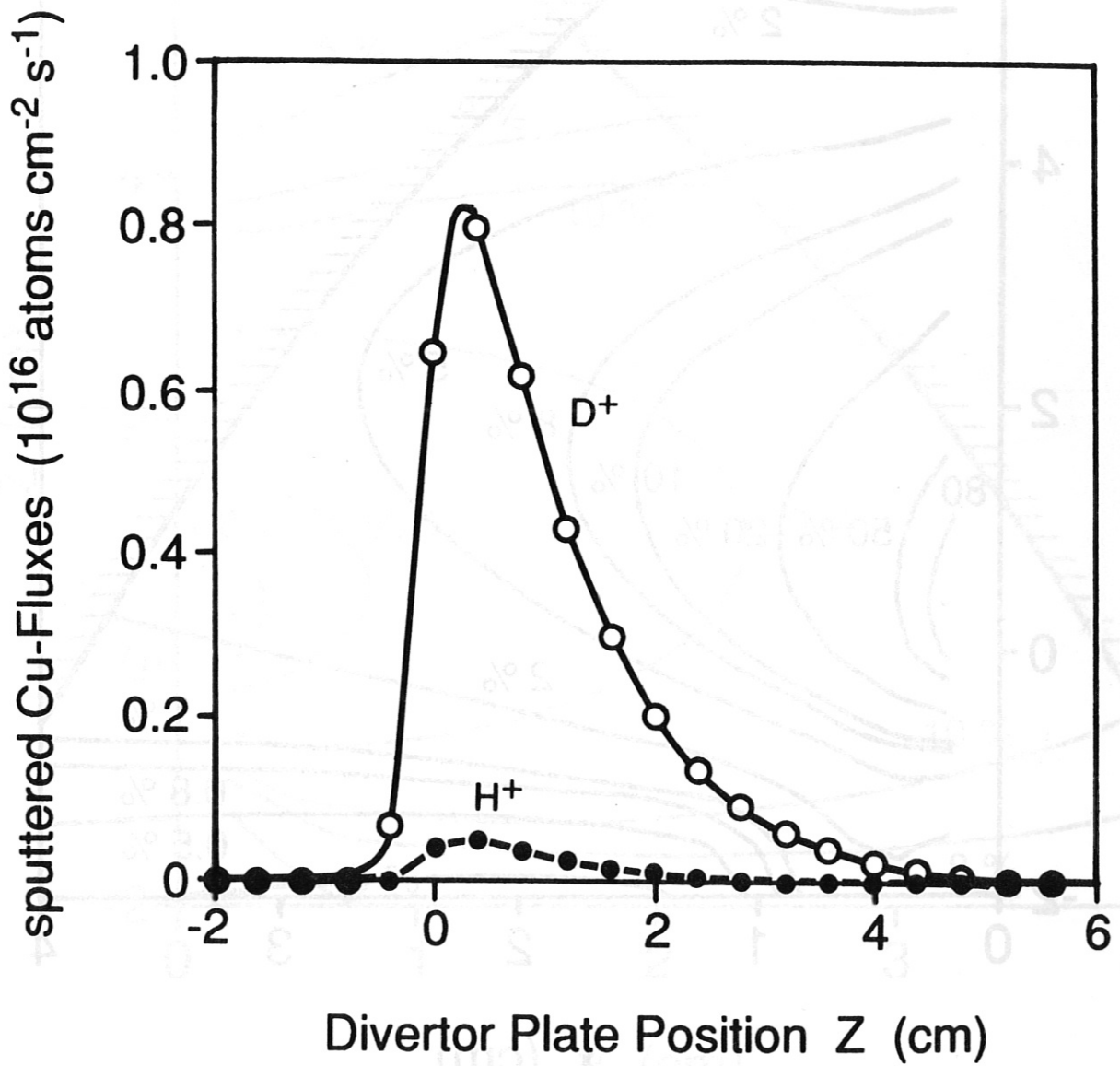
IPP 3 FSM 460 - 89

Z



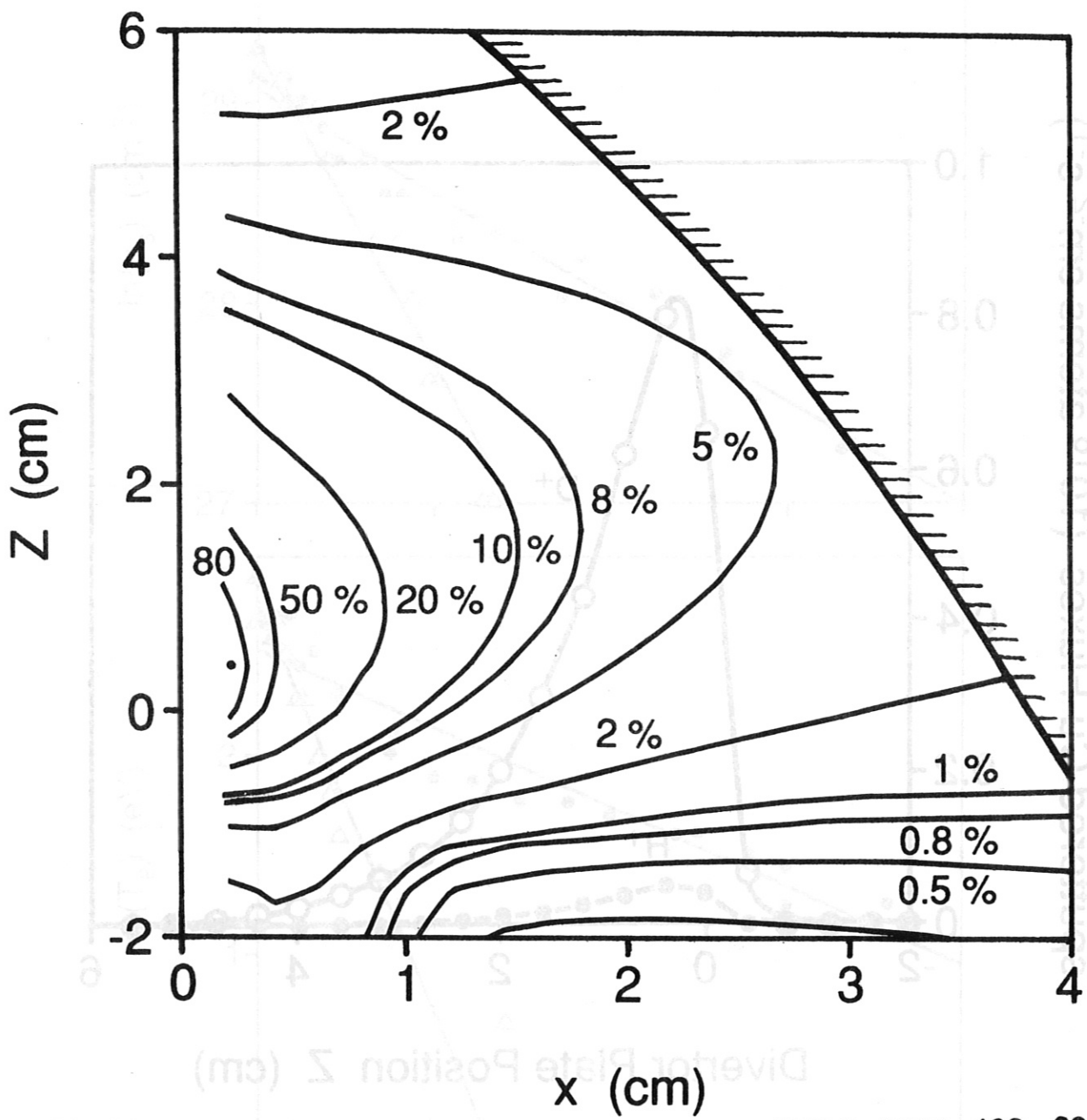
IPP 3 FSM 461 - 89

Fig. 11



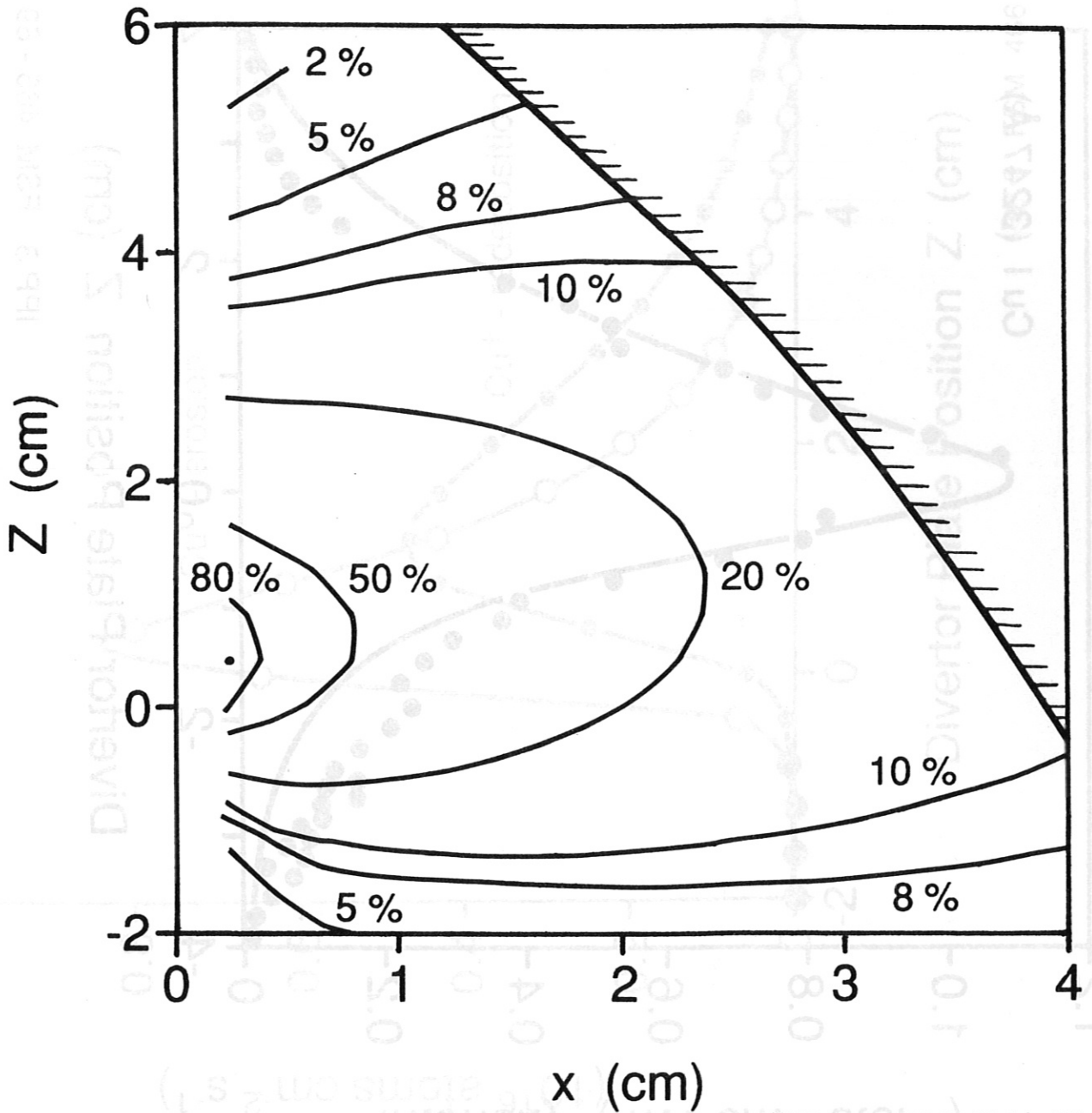
IPP 3 FSM 462 - 89

Fig. 12



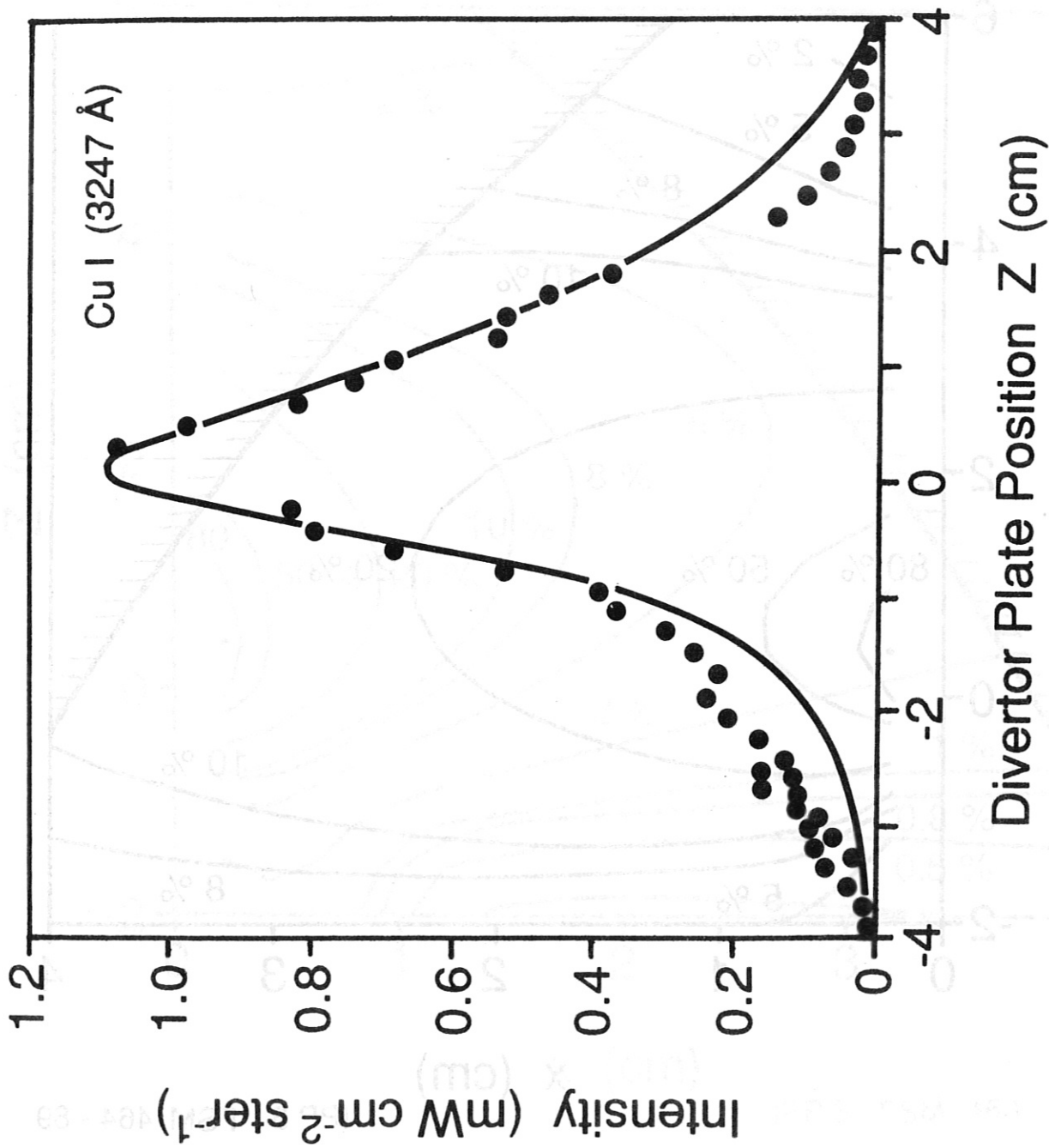
IPP 3 FSM 463 - 89

Fig. 13



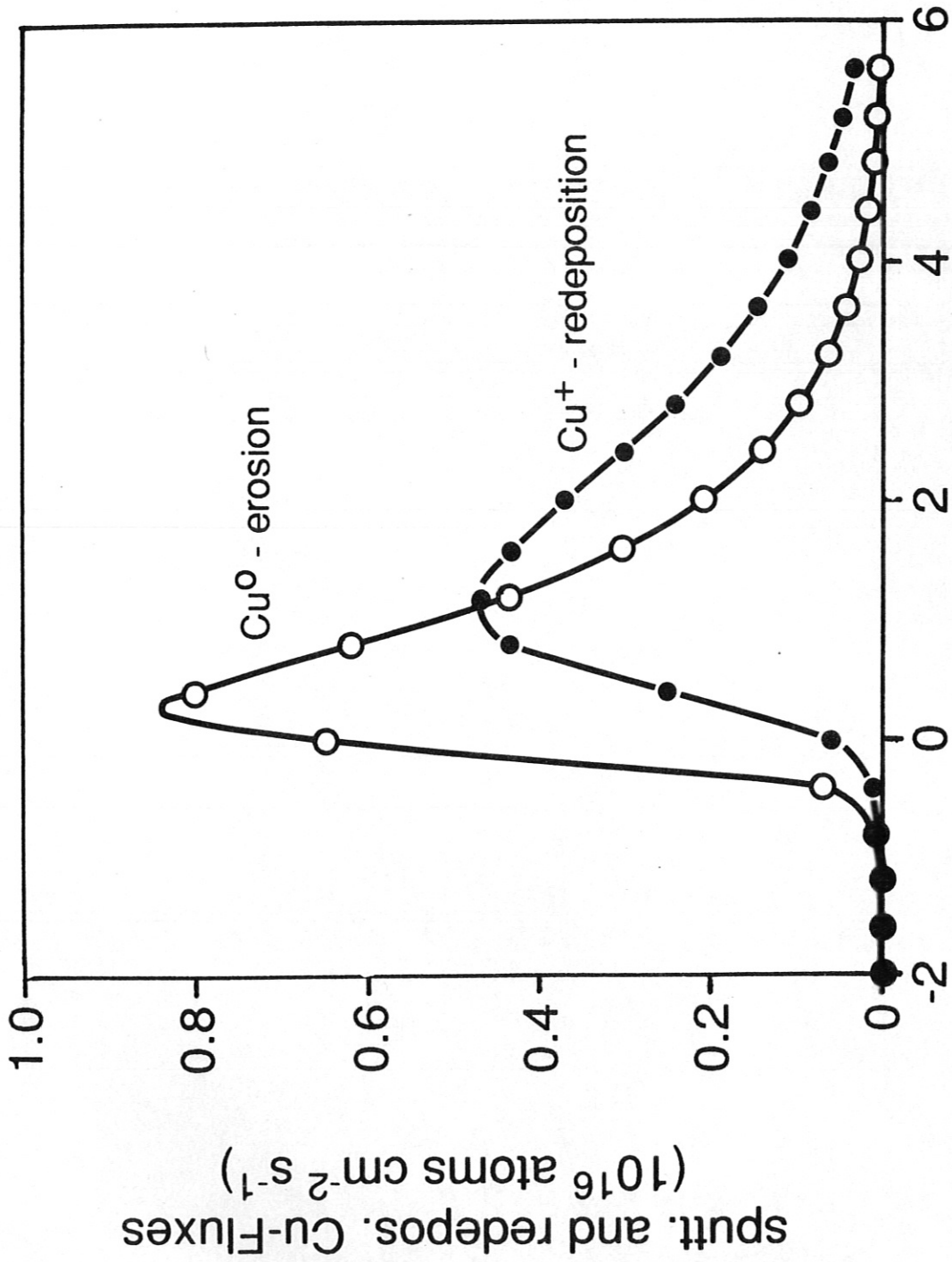
IPP 3 FSM 464 - 89

7. 14



IPP 3 FSM 465 - 89

Fig. 15



Divertor Plate Position Z (cm)